Discover Geoscience

Research

3D DEM-based analysis of cylindrical rock specimen failure and micro-fracturing: impact of stiffness and tensile strength

Zahra Mousavi[1] · **Milad Jabbarzadeh**[1]

Received: 6 November 2024 / Accepted: 17 February 2025
Published online: 25 February 2025

Abstract
Rock failure triggering with micro-fracturing poses significant challenges in engineering practices. In this study, the failure mechanism of the rock specimens was investigated focusing on the impact of stiffness and tensile strength on rock fracturing. To achieve this, uniaxial compression tests were simulated using the discrete element method for three rock types including granite, sandstone, and limestone. To enable elastic interactions at particle contacts for diverse rock material responses under stress, a linear parallel bond model was utilized. This model allows for elastic interactions while permitting slip, effectively simulating the complex behavior of rock materials under stress. The results revealed distinct mechanical behaviors among the three rock types, with granite exhibiting the highest peak stress and a steep stress–strain curve, indicative of its superior compressive strength. In contrast, sandstone shows lower peak stress and earlier failure due to its higher porosity and lower cohesion, while limestone demonstrates significant plastic deformation before failure, resulting in a more ductile response. Increased stiffness correlates with higher final strain values across all rock types, with limestone showing the greatest sensitivity to stiffness changes. The study demonstrates that increased tensile strength leads to higher peak stress and strain values, significantly delaying failure mechanisms, with a threefold increase in tensile strength resulting in a 1.47-fold increase in final stress for granite and a 2.46-fold increase for limestone. The analysis of crack development indicates that both stiffness and tensile strength substantially influence crack formation and distribution, particularly in sandstone.

Keywords DEM-based analysis · Rock failure · Micro-fracturing · Uniaxial compression test

1 Introduction

Rocks play a crucial role in geological and geotechnical engineering, serving as fundamental building blocks in various natural and man-made structures. Their mechanical properties are critical in applications ranging from the stability of slopes and tunnels to the extraction of natural resources [1–3]. The study of rock mechanics involves investigating the mechanical behavior of rock materials and rock masses. This field is essential for various engineering applications, including mining [4, 5], civil engineering [6–8], and petroleum engineering [9, 10]. Under various mechanical and environmental stresses, geological materials such as soils and rocks exhibit vulnerability to failure mechanisms, including cracking and deformation [11, 12]. These phenomena can significantly influence the mechanical properties of these materials, altering their deformation responses and overall stability [13–16]. The interplay between loading conditions and the inherent characteristics of geological substrates necessitates a comprehensive understanding of how such interactions affect

✉ Milad Jabbarzadeh, milad.jabbarzadeh@sharif.edu; Zahra Mousavi, zahra.s.moosavi@sharif.edu | [1]Department of Civil Engineering, Sharif University of Technology, Tehran, Iran.

structural integrity and geotechnical performance [17]. Hence, understanding the behavior of rock under different loading conditions is essential for predicting and mitigating potential failures that could have catastrophic consequences for infrastructure and the environment.

Extensive research has been conducted to understand the mechanical properties of rocks and their response to different loading conditions. Early studies focused on characterizing the fundamental properties of rocks, such as uniaxial compressive strength, tensile strength, and elasticity [18]. Over the years, more sophisticated testing methods and modeling techniques have been developed to gain deeper insights into rock behavior. One of the critical areas of research in rock mechanics is the failure behavior of rocks under mechanical loading conditions. Studies have shown that rocks can fail in different modes, including tensile and shear failures. For example, Griffith [19] developed the Griffith criterion, which describes the conditions under which brittle materials, such as rocks, fail under tensile stress. This criterion has been widely used to predict rock failure and has been extended to account for the presence of pre-existing flaws and cracks [20, 21].

Rocks are subjected to various loading conditions in nature and engineering applications. Mechanical loadings, such as uniaxial and triaxial compression tests, are commonly employed to study the failure behavior of rocks in laboratory settings, providing valuable insights into their strength and deformation characteristics [22]. A simplified empirical failure criterion, expressing rock strength at failure, was introduced by Shen et al. [23]. They proposed a new criterion for intact rock, allowing the calculation of the maximum effective principal stress at failure using the confining effective stress, UCS, and a dimensionless parameter. Zhang et al. [24] conducted triaxial tests on soil–rock mixture samples, revealing that high confining pressure causes large rock blocks to break, reducing strength. Samples with more large rock blocks had increased pore compression and volume shrinkage under low confining pressure, leading to denser mixtures after breakage. Moreover, Huang et al. [25] explored the mechanical behaviors and crack coalescence patterns of precracked sandstone samples using experimental and numerical methods. They found that flaw geometry significantly impacts deformation, strength, and failure, with stress–strain curves and coalescence patterns differing from those of intact specimens. In addition, Aladejare and Aladejare et al. [26, 27] evaluated the estimation of UCS from empirical equations, using point load strength, Schmidt rebound hardness, block punch index, porosity, and density as inputs. The study highlighted that the reliability of UCS estimations depends on the quality of input data and the rock type for which the empirical equations were developed, with point load strength being the most reliable index among the tests evaluated.

From the computational modeling perspective, Scholtès and Donzé [28] investigated the effect of grain interlocking on rock behavior using the Discrete Element Method (DEM). They demonstrated that the brittleness of rock is related to the degree of interlocking between particles, which affects tensile and compressive strength ratios and non-linear failure envelopes. Their model accurately reproduced brittle rock behavior, including fracturing processes, showing good agreement with laboratory tests. Furthermore, Zhang et al. [29] used coupled discrete element method and bonded particle method (DEM-BPM) to study porous rock mass properties. They found that UCS decreases with an increasing number of pores, while greater proportions of small pores increase UCS. Pore distribution affected fracture patterns, with fractures tending to develop along larger pores, resulting in lower UCS. Besides that, Xie et al. [30] examined the influence of soft interlayers on the failure mechanism of layered rock specimens under uniaxial compression using DEM simulations. They showed that soft interlayers significantly reduce UCS and cause strain softening, with thickness and dip angle of the interlayer influencing failure patterns. More recently, Zheng et al. [31] studied the mechanical properties and fracture evolution of Jinping marble under true triaxial stress using true triaxial tests, coupled particle flow code, and grain-based model (PFC3D-GBM) simulations. They observed that with increasing differential stress ($\sigma_2 - \sigma_3$), anisotropic deformation and intragranular tensile cracks increased, while peak strength and crack development patterns varied with confining pressures. Their study highlighted the progressive fracture characteristics and the importance of stress conditions on marble failure. Further research by Zheng et al. [32] on gabbro under true triaxial stress combined static–dynamic laboratory tests and numerical simulations. They identified distinct stages of disturbance failure and noted that increasing σ_1 or decreasing σ_2 and σ_3 affected the prevalence of intragranular and intergranular cracks. The acoustic emission activity pattern during failure aligned with the stages of deformation, and excavation disturbance increased the risk of deep fracture catastrophe.

Among rock mechanical properties, stiffness, and tensile strength are two critical parameters that significantly influence rock failure and micro-fracturing. Stiffness, often represented by the modulus of elasticity, determines the rock's ability to deform under applied stress. Rocks with higher stiffness exhibit less deformation, while those with lower stiffness are more prone to deformation and potential failure under the same loading conditions [33, 34]. Tensile strength is another vital property that governs the failure behavior of rocks. Unlike compressive strength, which is relatively high in most rocks, tensile strength is much lower and plays a crucial role in the initiation and propagation

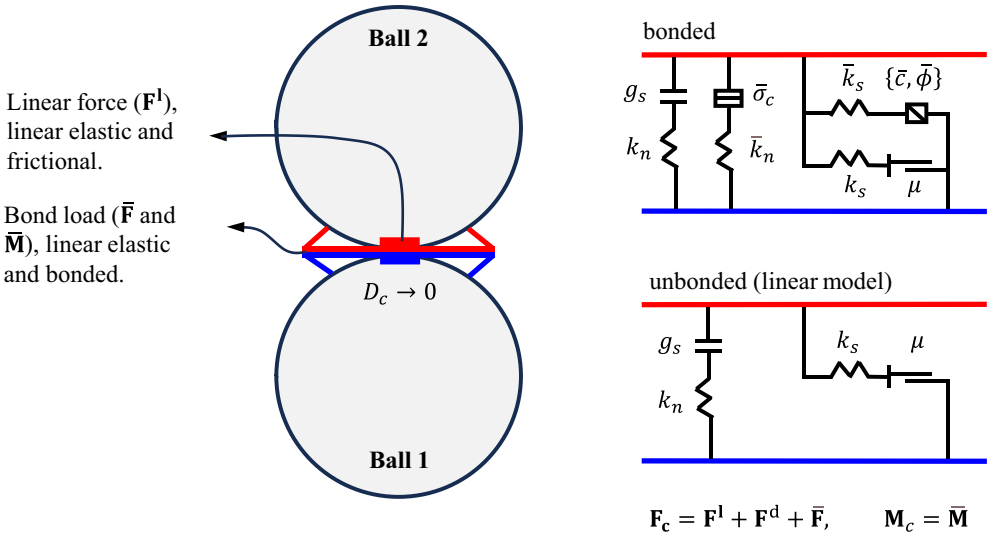

Fig. 1 Behavior and rheological components of the linear parallel bond model with inactive dashpots (modified after [39])

of cracks. When rocks are subjected to tensile stresses, even minor defects or pre-existing cracks can lead to failure [35]. Micro-fracturing, the process of small-scale crack initiation and propagation, is a precursor to macroscopic rock failure. Understanding the mechanisms of micro-fracturing is essential for predicting the onset of rock failure and implementing preventive measures, specifically under various stiffness and tensile strength conditions. The study of micro-fracturing involves advanced techniques such as acoustic emission monitoring, digital image correlation, and X-ray computed tomography [36, 37]. Effective rock maintenance strategies are crucial for ensuring the stability and longevity of rock structures. As an engineering application, rock slope stability is a critical concern in geotechnical engineering, particularly in areas with steep terrain and frequent human activity. The stability of rock slopes is influenced by various factors, including rock properties, slope geometry, and environmental conditions. Understanding the role of rock stiffness and tensile strength in micro-fracturing and failure of different rock types is essential for designing effective mitigation measures [38].

The purpose of this study is to conduct grain-scale modeling of rock failure and micro-fracturing under uniaxial compressive conditions, focusing on the influence of stiffness and tensile strength on rock behavior. The study aims to explore how these two key material properties affect the stress–strain response of rocks as they approach failure. Specifically, it investigates their role in the initiation and propagation of tensile and shear cracks, from a micro-mechanical perspective. By considering these parameters at the grain level, the research provides a more detailed understanding of fracture processes in rocks, which is crucial for accurately predicting rock behavior in various geotechnical applications. The insights gained from this study could have significant implications for the design and stability analysis of structures such as rock slopes, tunnels, and underground cavities, where understanding the fracture behavior of rocks is essential.

2 Discrete element model

2.1 Theoretical framework

In this study, the unconfined compression test was modeled to investigate the effects of variations in stiffness and tensile strength on the behavior of a cylindrical rock sample. The tests were simulated using the PFC^{3D} software based on the discrete element method. The linear parallel bond model [39] was employed to define the contact model between particles. The parallel bond element operates alongside the linear element, creating an elastic interaction between the pieces. The presence of a parallel bond does not prevent the occurrence of slip. These bonds are capable of transmitting both force and moment between the bodies. A parallel bond can be conceptualized as a collection of elastic springs with consistent normal and shear stiffness, uniformly distributed over a circular cross-section on the contact plane, centered at the contact point. These springs function in parallel with those of the linear element. When relative motion occurs at the contact point after the parallel bond is established, it induces a force and moment within the bond material. This

force and moment impact the two contacting bodies and correlate to the maximum normal and shear stresses at the bond periphery. If these maximum stresses surpass their respective bond strengths, the parallel bond fails, resulting in the removal of the bond material from the model along with its associated force, moment, and stiffnesses.

This model describes the behavior of two types of interfaces (Fig. 1):

(1) An infinitesimal, linear elastic (no-tension), frictional interface that can carry a force.
(2) A finite-size, linear elastic, bonded interface that can carry both a force and a moment.

The first interface operates similarly to the linear model, meaning it does not resist relative rotation and allows slip by applying a Coulomb limit to the shear force. The second interface, known as a parallel bond, functions in parallel with the first interface when bonded. This bonded interface resists relative rotation and exhibits linear elastic behavior until it reaches its strength limit. Once the strength limit is surpassed, the bond breaks and the interface become unbonded, at which point it can no longer carry any load. In its unbonded state, the linear parallel bond model behaves identically to the linear model.

The force–displacement law for the linear parallel bond model updates the contact force and moment:

$$\mathbf{F_c} = \mathbf{F^l} + \mathbf{F^d} + \overline{\mathbf{F}}, \mathbf{M}_c = \overline{\mathbf{M}} \tag{1}$$

where $\mathbf{F^l}$ is the linear force, $\mathbf{F^d}$ is the dashpot force, $\overline{\mathbf{F}}$ is the parallel-bond force, and $\overline{\mathbf{M}}$ is the parallel-bond moment. The linear and dashpot forces are updated as in the linear model, while the force and moment in the parallel bond are updated with different formulation.

The parallel-bond force is resolved into a normal and shear force, and the parallel-bond moment is resolved into a twisting and bending moment:

$$\overline{\mathbf{F}} = -\overline{F}_n \hat{\mathbf{n}}_\mathbf{c} + \overline{\mathbf{F}}_\mathbf{s} \tag{2}$$

$$\overline{\mathbf{M}} = \overline{M}_t \hat{\mathbf{n}}_\mathbf{c} + \overline{\mathbf{M}}_\mathbf{b} \tag{3}$$

where $\overline{F}_n > 0$ is tension. The parallel-bond shear force and bending moment lie on the contact plane and are expressed in the contact plane coordinate system:

$$\overline{\mathbf{F}}_\mathbf{s} = \overline{F}_{ss} \hat{\mathbf{s}}_\mathbf{c} + \overline{F}_{st} \hat{\mathbf{t}}_\mathbf{c} \tag{4}$$

$$\overline{\mathbf{M}}_\mathbf{b} = \overline{M}_{bs} \hat{\mathbf{s}}_\mathbf{c} + \overline{M}_{bt} \hat{\mathbf{t}}_\mathbf{c} \tag{5}$$

When a parallel bond is formed using the bond method, it establishes an interface between two notional surfaces, and both the parallel-bond force and moment are set to zero initially. This parallel bond creates an elastic interaction between the two notional surfaces, which is eliminated when the bond breaks.

The parallel-bond surface gap accumulates through the relative normal displacement of the piece surfaces, expressed as:

$$\overline{\mathrm{g}}_s = \sum \Delta\delta_n \tag{6}$$

where $\Delta\delta_n$ represents the incremental change in normal displacement.

The force–displacement relationship for the parallel-bond force and moment is described in seven steps. Firstly, the bond cross-sectional properties are updated as:

$$\overline{R} = \overline{\lambda} \begin{cases} \min\left(R^{(1)}, R^{(2)}\right) & \text{ball-ball} \\ R^{(1)} & \text{ball-facet} \end{cases} \tag{7}$$

$$\overline{A} = \pi \overline{R}^2, \overline{I} = \frac{1}{4}\pi \overline{R}^4, \overline{J} = \frac{1}{2}\pi \overline{R}^4 \tag{8}$$

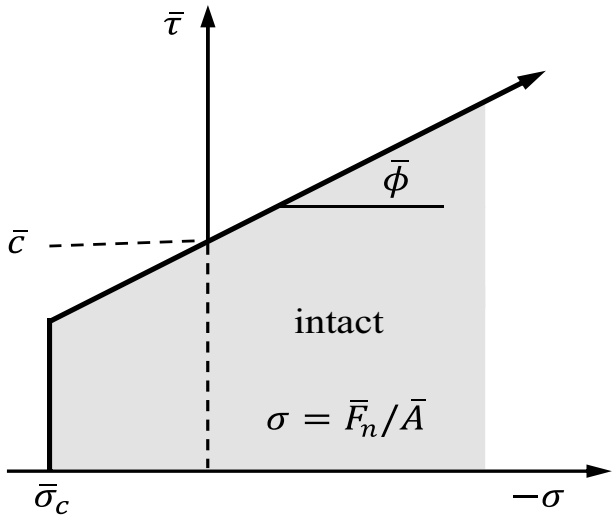

Fig. 2 Failure envelope for the parallel bond (modified after [39])

where $\bar{A}$ is the cross-sectional area, $\bar{I}$ is the moment of inertia of the parallel bond's cross section (about the line passing through $\mathbf{x_c}$ and in the direction of $\overline{\mathbf{M}}_\mathbf{b}$), and $\bar{J}$ is the polar moment of inertia of the parallel bond cross section (about the line passing through $\mathbf{x_c}$ and in the direction of $\hat{\mathbf{n}}_\mathbf{c}$). The bond cross section is circular in 3D modeling.

Secondly, the normal force is updated according to the normal-force update mode:

$$\bar{F}_n := \bar{F}_n + \bar{k}_n \bar{A} \Delta\delta_n \tag{9}$$

Thirdly, the shear force is updated as:

$$\overline{\mathbf{F}}_\mathbf{s} := \overline{\mathbf{F}}_\mathbf{s} - \bar{k}_s \bar{A} \Delta\boldsymbol{\delta}_\mathbf{s} \tag{10}$$

where $\Delta\boldsymbol{\delta}_\mathbf{s}$ is the relative shear displacement increment.

Fourthly, the torsional moment is updated as:

$$\bar{M}_t := \bar{M}_t - \bar{k}_s \bar{J} \Delta\theta_t \tag{11}$$

where $\Delta\theta_t$ is the relative twist-rotation increment. The torsional stiffness (k_t) for a twisted elastic circular shaft of length (L) subjected to equal and opposite twisting moments is given by:

$$M_t = k_t \theta_t \tag{12}$$

$$k_t = \frac{GJ}{L} \tag{13}$$

where G is the shear modulus and J is the polar moment of inertia of the cross-sectional area about the axis of the shaft. The moment-twist relation of Eq. (11) is obtained by setting $k_t = \bar{k}_s \bar{J}$.

Fifthly, the bending moment is updated as:

$$\overline{\mathbf{M}}_\mathbf{b} := \overline{\mathbf{M}}_\mathbf{b} - \bar{k}_n \bar{I} \Delta\boldsymbol{\theta}_\mathbf{b} \tag{14}$$

where $\Delta\boldsymbol{\theta}_\mathbf{b}$ is the relative bend-rotation increment. The bending stiffness (k_b) for an elastic symmetrical beam of length (L) subjected to equal and opposite bending moments is given by:

$$M_b = k_b \theta_b \tag{15}$$

$$k_b = \frac{EI}{L} \tag{16}$$

where E is the Young's modulus and I is the moment of inertia of the cross-sectional area about the neutral axis of the beam. The moment-twist relation of Eq. (14) is obtained by setting $k_b = \bar{k}_n \bar{I}$.

Next step is updating the maximum normal ($\bar{\sigma} > 0$ is tension) and shear stresses at the parallel-bond periphery:

$$\bar{\sigma} = \frac{\bar{F}_n}{\bar{A}} + \bar{\beta}\frac{||\bar{\mathbf{M}}_\mathbf{b}||\bar{R}}{\bar{I}} \tag{17}$$

$$\bar{\tau} = \frac{||\bar{\mathbf{F}}_\mathbf{s}||}{\bar{A}} + \bar{\beta}\frac{|\bar{M}_t|\bar{R}}{\bar{J}} \tag{18}$$

The moment-contribution factor ($\bar{\beta} \in [0,1]$) was discussed in detail by Potyondy [40].

Finally, the strength limits are enforced as shown in Fig. 2. If the tensile strength limit is exceeded ($\bar{\sigma} > \bar{\sigma}_c$), the bond breaks in tension. If the bond remains intact, the shear strength limit is enforced. The shear strength ($\bar{\tau}_c = \bar{c} - \sigma \tan\bar{\phi}$), where $\sigma = \bar{F}_n/\bar{A}$ is the average normal stress acting on the parallel bond cross-section. If the shear strength limit is exceeded, the bond breaks in shear.

The linear parallel bond model divides energy into four categories. Strain energy (E_k) is the energy stored in the linear springs with the range of $[0, +\infty)$. The strain energy is updated as:

$$\mathrm{E}_k = \frac{1}{2}\left(\frac{\left(F_n^l\right)^2}{k_n} + \frac{||\mathbf{F}_\mathbf{s}^\mathbf{l}||^2}{k_s}\right) \tag{19}$$

Slip energy (E_μ) is the total energy dissipated due to frictional slip with the range of $(-\infty, 0]$. The slip energy is updated as:

$$E_\mu := E_\mu - \frac{1}{2}\left(\left(\mathbf{F}_\mathrm{s}^\mathrm{l}\right)_o + \mathbf{F}_\mathrm{s}^\mathrm{l}\right) \cdot \Delta\boldsymbol{\delta}_\mathrm{s}^\mu \tag{20}$$

$$\Delta\boldsymbol{\delta}_\mathrm{s}^\mu = \Delta\boldsymbol{\delta}_\mathrm{s} - \Delta\boldsymbol{\delta}_\mathrm{s}^k = \Delta\boldsymbol{\delta}_\mathrm{s} - \left(\frac{\mathbf{F}_\mathrm{s}^\mathrm{l} - \left(\mathbf{F}_\mathrm{s}^\mathrm{s}\right)_o}{k_\mathrm{s}}\right) \tag{21}$$

where $\left(\mathbf{F}_\mathrm{s}^\mathrm{l}\right)_o$ is the linear shear force at the start of the timestep. The adjusted relative shear-displacement increment is decomposed into two parts: an elastic component ($\Delta\boldsymbol{\delta}_\mathrm{s}^k$) and a slip component ($\Delta\boldsymbol{\delta}_\mathrm{s}^\mu$). The slip energy increment is obtained by taking the dot product of the slip component with the average linear shear force over the duration of the timestep. The slip energy remains zero until the bond breaks. Once the bond is broken, slip energy begins to accumulate as a result of the relative shear displacements between the particles.

Dashpot energy (E_β) represents the total energy dissipated by the dashpots with the range of $(-\infty, 0]$. The dashpot energy is updated as:

$$E_\beta := E_\beta - \mathbf{F}^\mathbf{d} \cdot \left(\dot{\boldsymbol{\delta}}\Delta t\right) \tag{22}$$

where $\dot{\boldsymbol{\delta}}$ is the relative translational velocity.

Table 1 Properties of the rocks utilized in the simulations

Parameter	Rock type		
	Granite	Sandstone	Limestone
Porosity	0.01	0.15	0.1
Density (kg/m^3)	2650	2300	2600
Linear stiffness of particles (GPa)	50	30	20
Stiffness of bond material (GPa)	50	30	20
Tensile strength (MPa)	10	5	4
Cohesion (MPa)	50	20	35
Friction coefficient	0.7	0.6	0.5

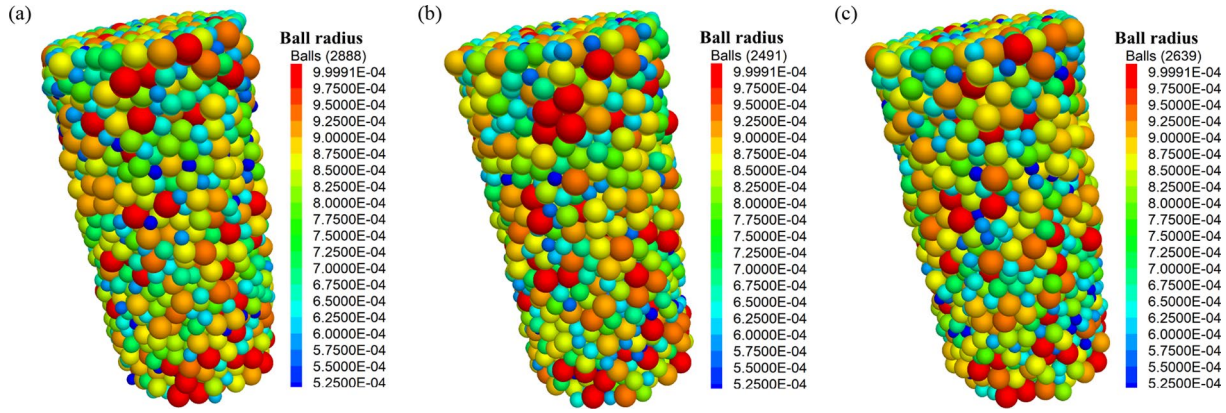

Fig. 3 Geometry and ball radius distribution of simulated samples: **a** Granite, **b** Sandstone, **c** Limestone

Table 2 The scenarios of tensile strength and stiffness parameters

Rock type	Tensile strength (MPa)	Stiffness (GPa)
Granite	5	30
	10	50
	15	70
Sandstone	2.5	20
	5	30
	7.5	40
Limestone	2	10
	4	20
	6	30

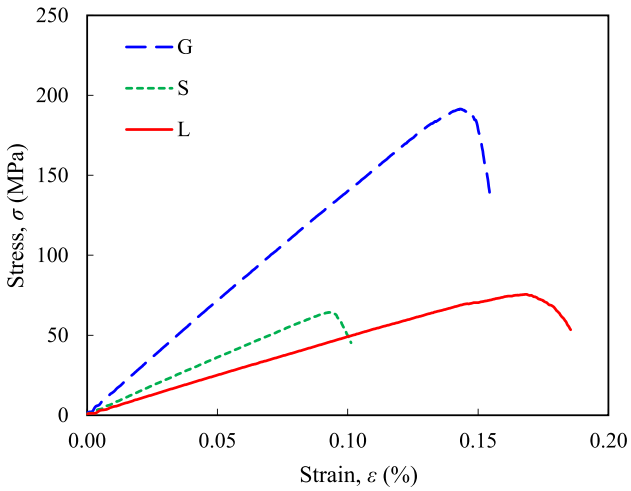

Fig. 4 The comparison of stress–strain behavior of the utilized materials

Bond strain energy ($\bar{E}_k$) is the energy stored within the parallel-bond springs with the range of [0, +∞). The bond strain energy is updated as:

$$\bar{E}_k = \frac{1}{2}\left(\frac{\bar{F}_n^2}{\bar{k}_n\bar{A}} + \frac{||\bar{\mathbf{F}}_\mathbf{s}||^2}{\bar{k}_s\bar{A}} + \frac{\bar{M}_t^2}{\bar{k}_s\bar{J}} + \frac{||\bar{\mathbf{M}}_\mathbf{b}||^2}{\bar{k}_n\bar{I}}\right) \tag{23}$$

2.2 Numerical model and input parameters

The rock particles were modeled as balls capable of overlapping, with diameters ranging from 0.5 mm to 1 mm. The simulated samples were modeled in a cylindrical shape by ASTM standard [41]. Tuncay and Hasancebi [42] researched to investigate the effect of the height-to-diameter ratio (H/D) of rock samples on their UCS. Their results indicated that high UCS values are obtained for H/D lower than 2, a very slight difference in values between 2 and 2.5, and UCS remains effectively constant with a H/D higher than 2.5. However, the ASTM guidelines recommend an H/D ratio of 2–2.5, while the ISRM code suggests a range of 2.5–3. Based on these findings, the optimal ratio chosen for this study was established as 2. Based on this, the diameter and height of the sample were chosen to be 15 and 30 mm, respectively.

In the modeling process, three types of material with distinct mechanical properties were utilized. The properties of the materials were selected to ensure that each one closely resembled a commonly used rock in geotechnical applications. These materials, whose properties are detailed in the Table 1, represent granite (G), sandstone (S), and limestone (L). The DEM model utilized in this study incorporates key microstructural parameters as outlined in Table 1. These parameters govern the inter-particle interactions and bond behavior, directly influencing the macroscopic strength and failure characteristics of the rock specimens. For example, the tensile strength and cohesion determine the bond-breaking threshold under stress, while stiffness properties dictate the deformation response. The microstructural configuration, as defined by these parameters, significantly impacts the observed fracturing patterns and failure modes.

The microstructural parameters of the model were selected based on the theoretical framework of the Linear Parallel Bond Model. In this approach, the strength of rock samples is represented by their failure mechanisms, which initiate microscopically as interactions between grains lead to sliding and micro-crack formation. These micro-cracks coalesce into macroscopic fractures as stress increases. During the simulation of uniaxial compression, the defined material properties govern the evolution of stress and strain, with failure occurring at 0.7 times the peak stress. The model calculates forces, moments, and particle interactions at each time step, updating particle positions in a three-dimensional coordinate system. This micro-mechanical modeling approach captures the transition from microstructural deformation to macroscopic failure, linking the defined parameters to the observed strength and behavior of the rock samples.

Due to the varying densities of these materials, the number of balls created in each model differs, and a view of the geometry of each model is presented in Fig. 3. At the top and bottom of the cylindrical samples, two walls were positioned to apply the load. These walls moved towards each other at a speed of 0.1 m/s, subjecting the samples to compressive loading. During the tests, the number of tensile and shear cracks formed at various stages of the experiment, as well as the stress–strain behavior of the samples, were monitored. To achieve a more precise analysis, the modeling was conducted in four distinct groups. In the first group, the overall behavior of the various materials, as detailed in Table 1, was compared. In this study, in addition to comparing the behavior of the materials with each

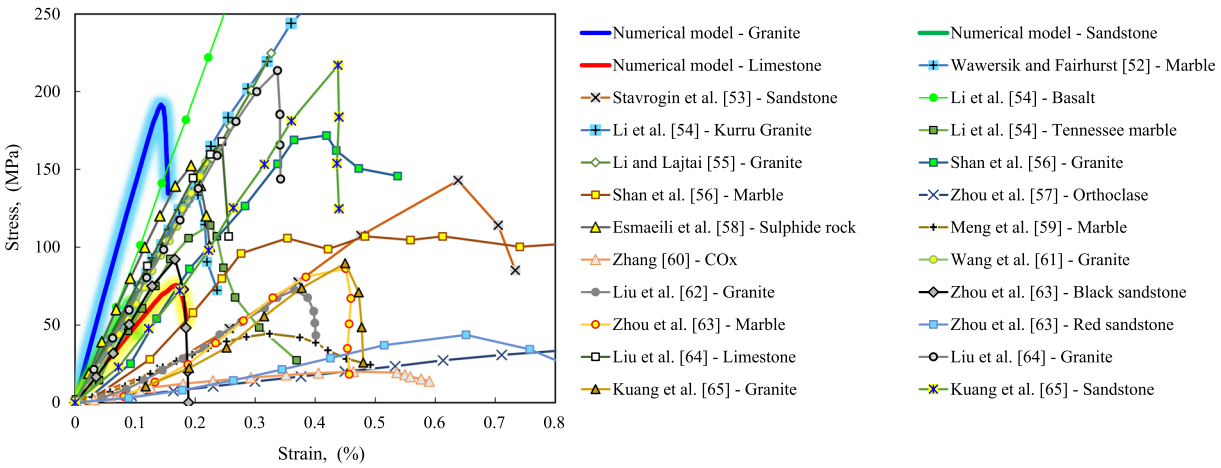

Fig. 5 The comparison of stress–strain curve for different rocks

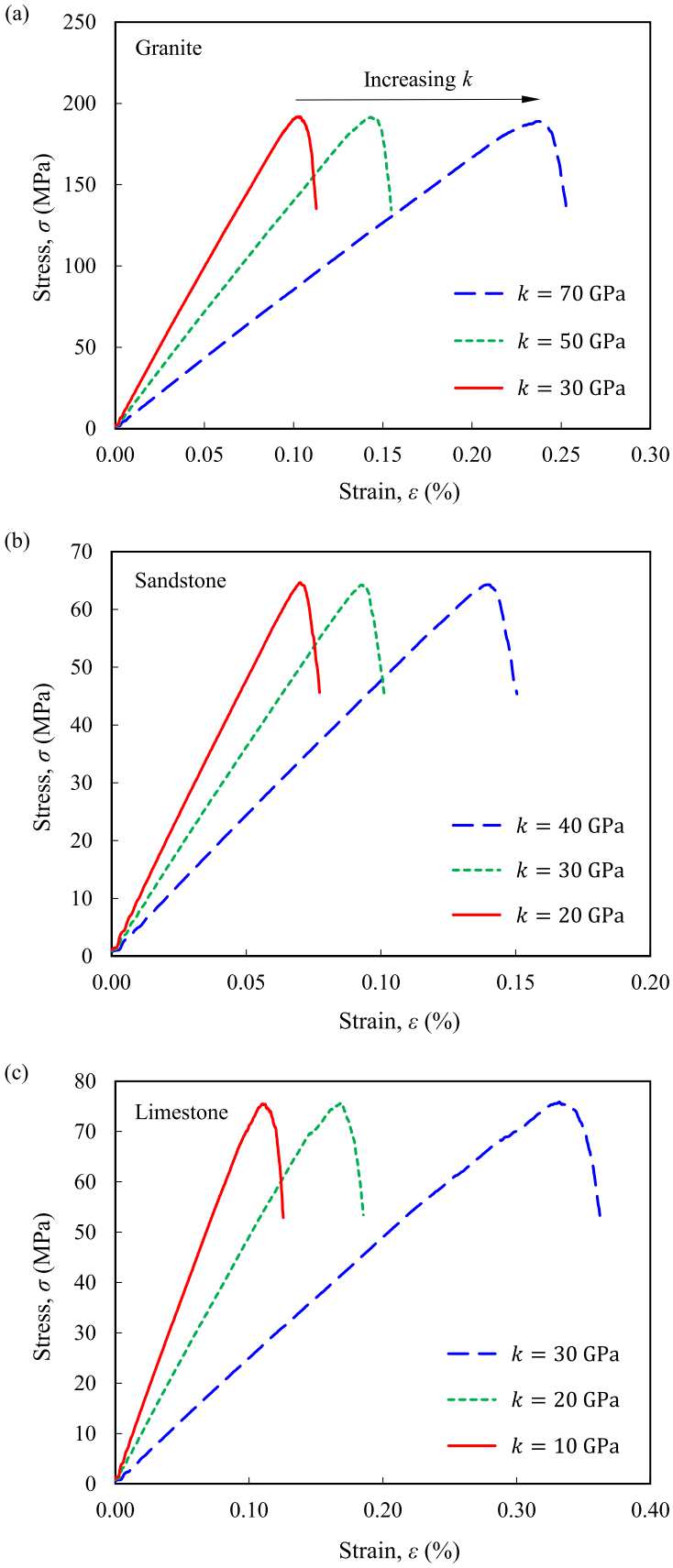

Fig. 6 The effect of stiffness on the stress–strain behavior of **a** Granite, **b** Sandstone, and **c** Limestone

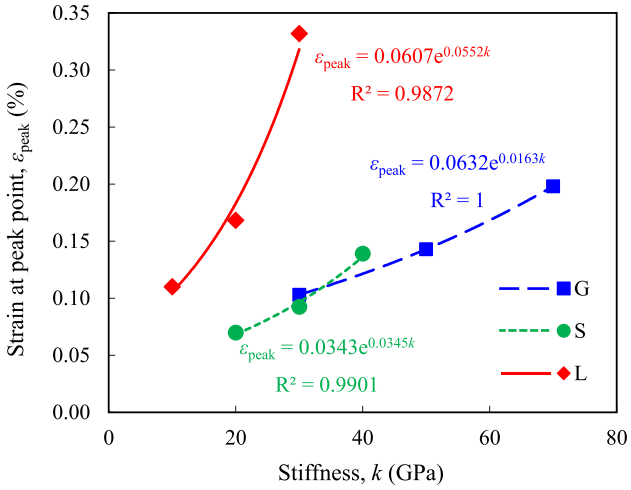

Fig. 7 The dependency of strain at peak point on stiffness

other, the effect of changes in stiffness and tensile strength on stress–strain behavior and the initiation and propagation of cracking was investigated with a parametric study. The modeling scenarios are presented in Table 2. The properties of the materials used in this study were selected based on relevant literature, including granite [43–45], sandstone [46–48], and limestone [49–51].

3 Results and discussion

3.1 Stress–strain behavior

The distinct behavior of each material under uniaxial compression test was illustrated in Fig. 4. As shown in Fig. 4, all three materials display softening behavior before failure, although the slope of their stress–strain curves differs significantly. Granite demonstrates the highest peak stress and a steeper stress–strain curve, reflecting its superior compressive strength and stiffness compared to sandstone and limestone. Its interlocking structure facilitates effective load distribution, enabling granite to achieve high peak stresses before failure. Additionally, after experiencing peak stress (σ_{peak}), granite shows a steeper decline in stress compared to other materials. In contrast, sandstone demonstrates the lowest σ_{peak} and fails at a lower level of stress and strain compared to granite. However, it exhibits a steeper stress–strain curve than limestone. This behavior is primarily influenced by its higher porosity and lower cohesion. Higher porosity typically results in decreased strength due to presence of the voids that do not contribute to load-bearing capacity. Moreover, limestone exhibits lower σ_{peak} and a more gradual stress–strain curve than sandstone. Its capacity for significant plastic deformation before reaching peak stress contributes to the less steep slope of its stress–strain curve. This characteristic enables limestone to absorb more energy prior to failure, resulting in a more ductile response. Consequently, limestone tends to fail through a combination of brittle and ductile mechanisms, leading to a slower transition from elastic to plastic behavior compared to sandstone.

Figure 5 illustrates the comparison of stress–strain curves for various types of rocks. It is evident that the stress–strain curves for all rock types are confined to a limited range. In fact, rocks exhibit only a narrow range of stress and strain variations, and the numerical model results from this study fall within this range. This alignment allows for the validation of the model against findings from other research. However, it is important to note that the stress–strain behavior is not entirely consistent, even among the same rock types. This variability can be attributed to differences in mechanical properties caused by factors such as mineral composition, sampling conditions, the presence of primary cracks, and variations in experimental or numerical methodologies used.

3.1.1 The role of stiffness

Figure 6 illustrates the role of stiffness in the stress–strain behavior of rock samples. The results show that an increase in stiffness leads to failure at higher final strain (ε_f) values with approximately equal σ_{peak}. For example, for granite samples 2.3 times increase in stiffness from 30 to 70 GPa results in 2.25 times increase in final strain. Similarly, sandstone shows

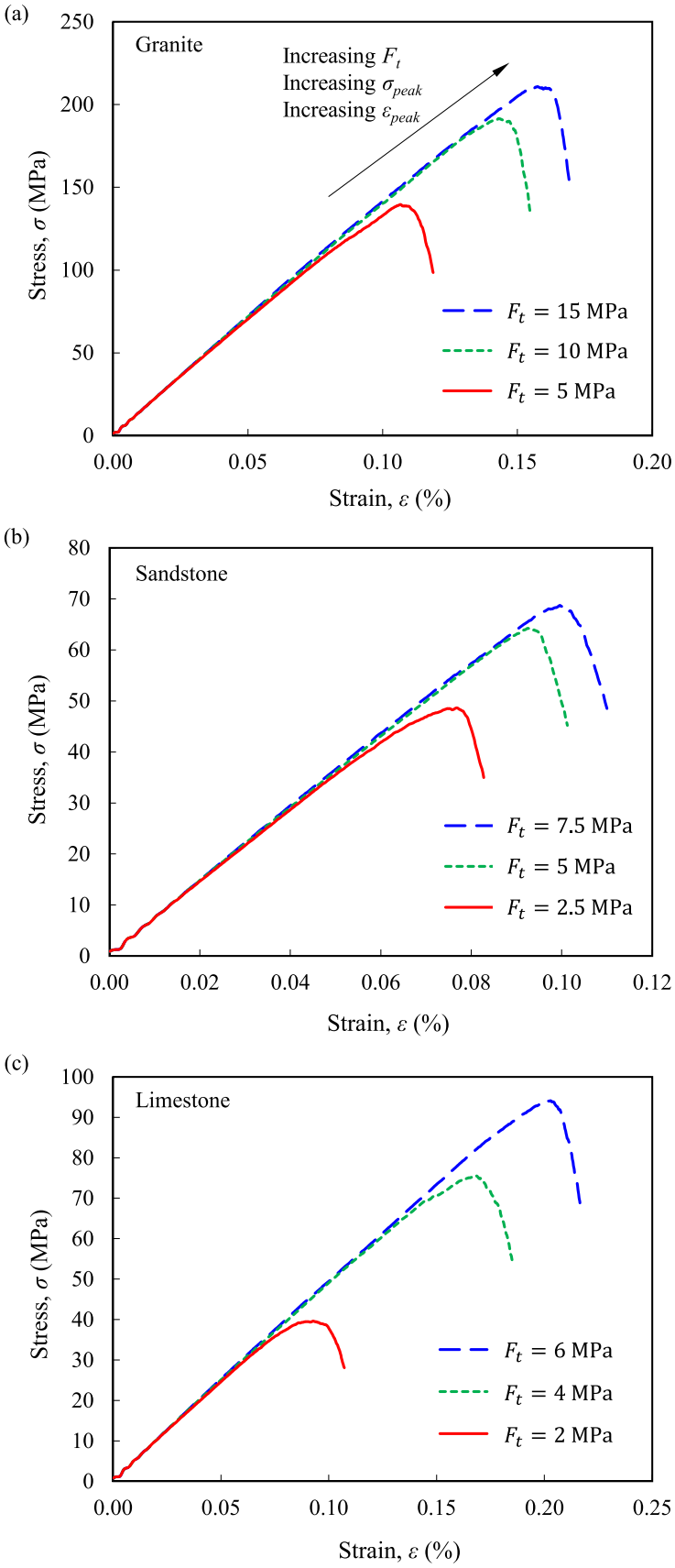

Fig. 8 The effect of variations in tensile strength on the stress–strain behavior of **a** Granite, **b** Sandstone, and **c** Limestone

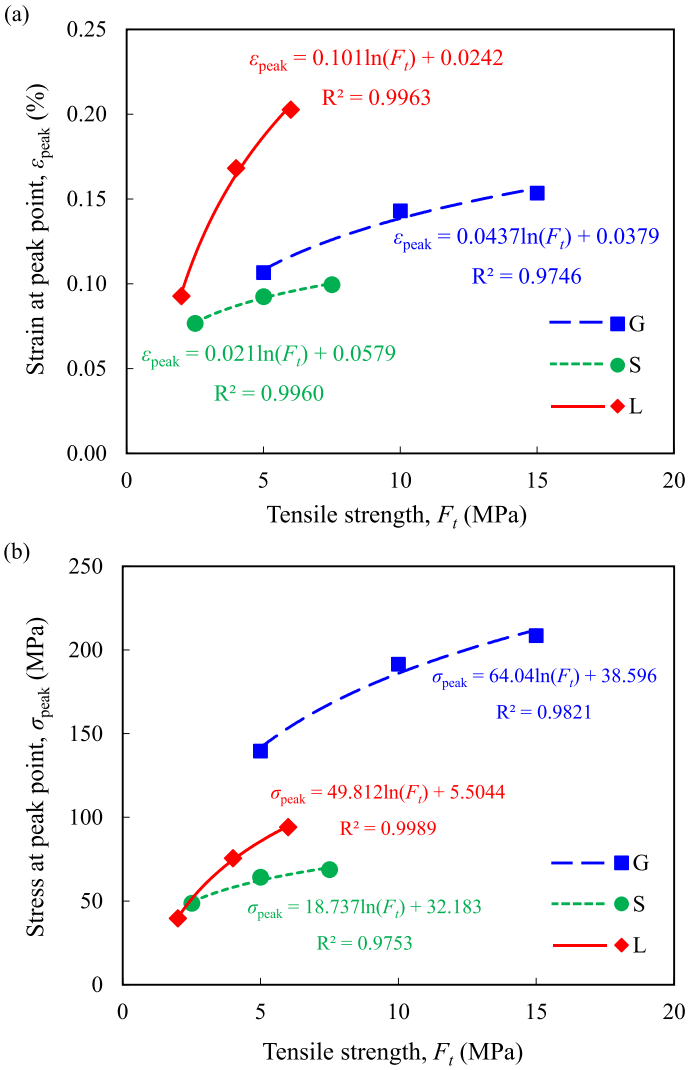

Fig. 9 The dependency of **a** strain at peak point and **b** stress at peak point on tensile strength

1.95 times increase in final strain with a twofold increase in stiffness, while limestone exhibits 2.89 times increase in final strain with a threefold increase in stiffness. This shows a linear relationship between rock stiffness and ε_f.

The observed behavior can be attributed to their distinct material properties and failure mechanisms. Granite, being brittle, shows a nearly proportional increase in ε_f with increased stiffness due to its ability to sustain higher stress before fracture. Sandstone, with its weaker cementing materials and higher porosity, exhibits a less pronounced increase in ε_f as its structure leads to earlier micro-cracking and failure. Limestone, being more ductile, shows the most significant increase in ε_f with increased stiffness, as its plastic deformation capability allows it to accommodate more strain before failure. It should be noted that with an increase in stiffness, the σ_{peak} does not change significantly, being 191 MPa for granite, 64 MPa for sandstone, and 75 MPa for limestone, but the corresponding peak strain (ε_{peak}) increases. Figure 7 shows the dependency of ε_{peak} on stiffness. The presented predictive relationships indicate that, for all materials, the ε_{peak} changes exponentially with increasing stiffness. Notably, the slope of these variations for limestone is 3.4 times greater than that of granite, highlighting the significant differences in the physical properties and mechanical behavior of these materials. This relationship underscores the greater sensitivity of limestone to changes in stiffness, which contributes to its unique ductile behavior compared to the more brittle nature of granite.

As it is evident from the results, higher stiffness leads to less deformation under applied loads. This means that the rock can withstand greater stresses without significant changes in shape, which helps prevent the initiation of micro-cracks. Moreover, stiffer materials can better distribute the applied load across their structure. This reduces localized stress concentrations, which are often the precursors to micro-fracturing. Besides that, increased stiffness often correlates

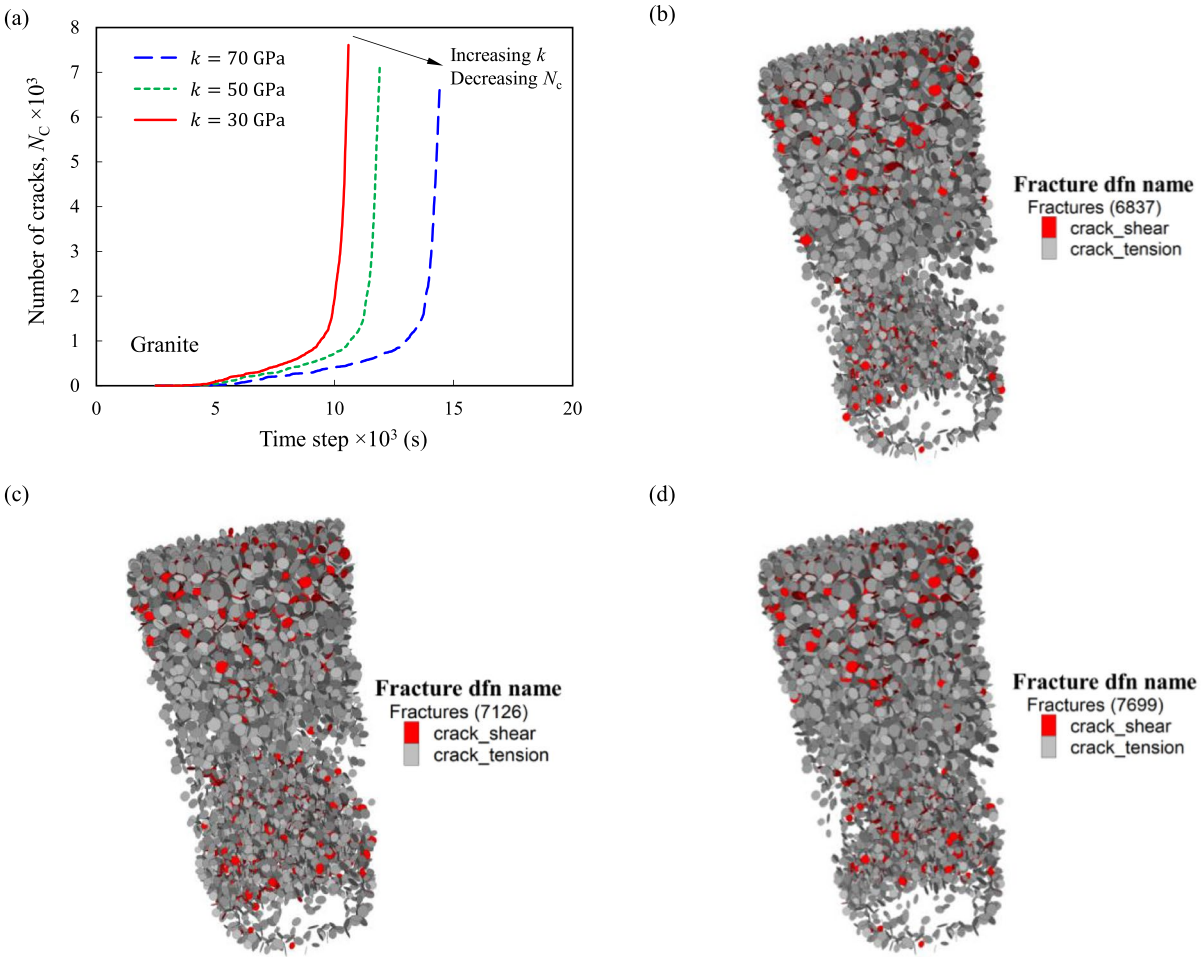

Fig. 10 **a** The effect of stiffness on crack propagation in granite samples, and fracture distribution in samples with stiffness of **b** 70 GPa, **c** 50 GPa, and **d** 30 GPa

with stronger inter-particle bonds within the rock matrix. This improves the overall integrity of the rock, making it more resistant to micro-scale failures.

3.1.2 The role of tensile strength

According to Fig. 8, an increase in tensile strength (F_t) results in higher stress and strain values at both the peak and final points of the stress–strain curves for all samples. However, the rate of change in these curves varies among the different materials due to their unique characteristics. As shown in Fig. 8a, a threefold increase in F_t of granite specimens (from 5 to 15 MPa), results in 1.47 times increase in final stress (σ_f) and 1.43 times increase in ε_f. This increased capacity for energy absorption and deformation reflects granite's effective stress redistribution, which mitigates micro-crack development. Moreover, sandstone, with its lower stiffness and more fragile composition, shows moderate increases in σ_f being 1.39 times and ε_f being 1.33 times, with a threefold increase in F_t.

Limestone demonstrates the most significant response to increases in tensile strength, with σ_f increasing by 2.46 times and ε_f by 2.02 times. As it is evident from the findings, increased tensile strength can delay the onset of failure mechanisms such as shear sliding or tensile cracking. This allows the rock to accommodate greater loads before reaching its failure point. Additionally, rocks with higher tensile strength can absorb more energy before failing. This allows them to withstand higher loads and dissipate energy more effectively, reducing the likelihood of sudden failures.

Furthermore, Fig. 9 illustrates the trends of σ_{Peak} and ε_{Peak} in relation to F_t. Unlike the exponential changes observed in ε_{Peak} concerning stiffness, the variables shown in Fig. 9 exhibit logarithmic increases. It suggests that the changes in σ_{Peak} and ε_{Peak} will finally reach a state of equilibrium. As noted previously, the rate of change for limestone is greater

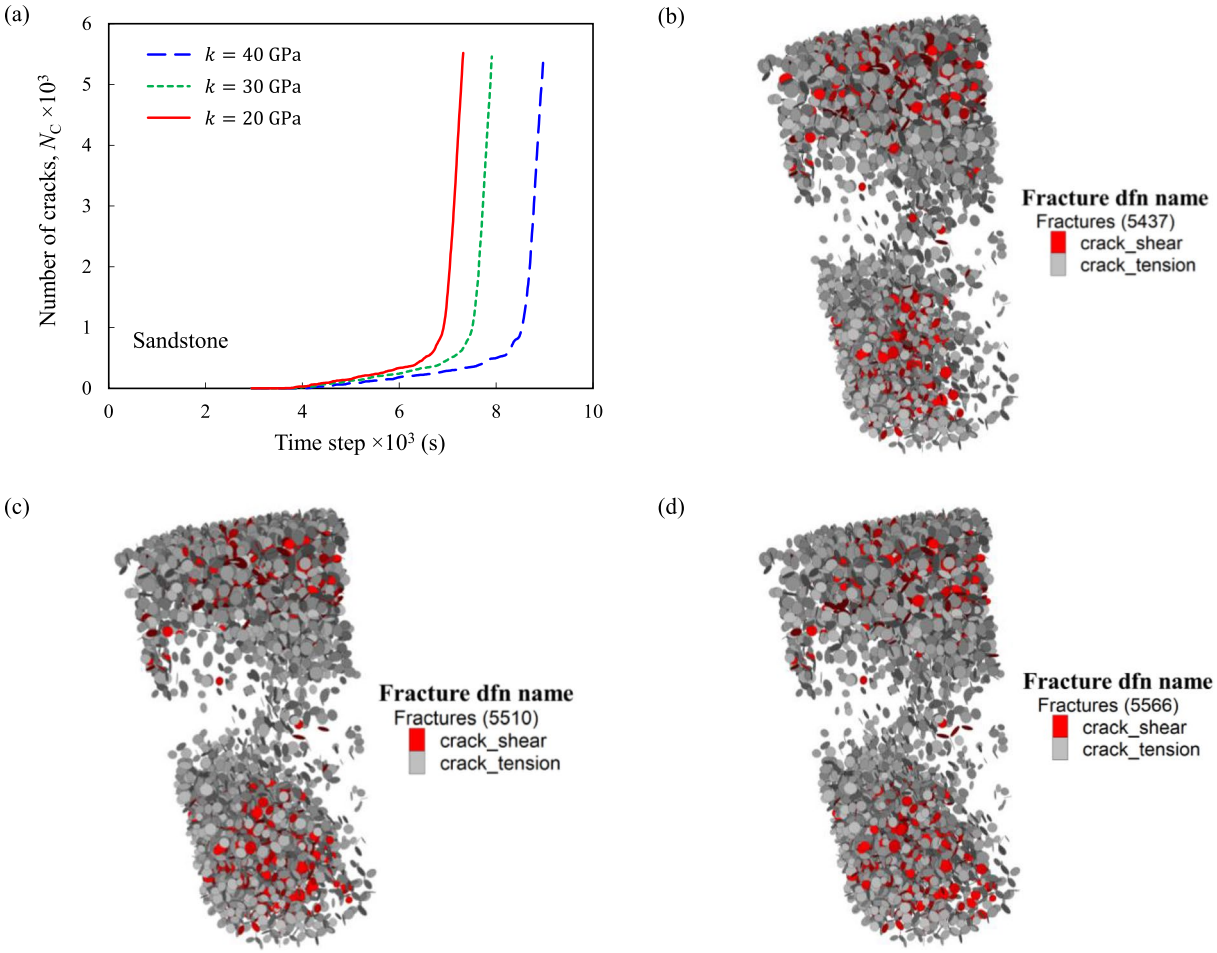

Fig. 11 **a** The effect of stiffness on crack propagation in sandstone samples, and fracture distribution in samples with stiffness of **b** 40 GPa, **c** 30 GPa, and **d** 20 GPa

than that of the other materials. Finally, based on the trends observed, relationships between peak stress and peak strain concerning F_t were estimated which are presented in Fig. 9.

3.2 Crack initiation and propagation

3.2.1 The role of stiffness

The impact of stiffness on the initiation and distribution of micro-cracks in a granite sample is illustrated in Fig. 10. As observed, the trend of changes in the number of cracks (N_c) over time follows a bilinear relationship. Initially, cracking starts at a mild rate and then intensifies progressively over time. According to the results, with an increase in stiffness, the rate of crack development decreases in both phases, and the final maximum number of cracks ($N_{c,max}$) also shows a reduction. As depicted in Fig. 10a, cracking in granite samples with stiffness values of 30, 50, and 70 GPa begins after 3620, 3830, and 4220 s, respectively, from the start of the test. Moreover, an increase in stiffness results in a reduction in both the total N_c and their occurrence at specific time steps. This means that with an increase in the stiffness of the rock, it takes longer to enter the second phase, which is characterized by the progressive growth of cracking.

For instance, at 10,000 s, the number of cracks in the sample with a stiffness of 30 GPa is 1739, whereas in samples with stiffnesses of 50 and 70 GPa, the numbers are 735 and 421, respectively. Figure 10b–d display the differentiated tension and shear cracked interfaces between the balls. According to Fig. 10, the majority of the cracks are tension cracks, predominantly located in the upper half of the granite samples.

Figure 11 illustrates the effect of variations in stiffness on the cracking of the sandstone samples. As depicted in Fig. 11a, cracking in sandstone samples with stiffness values of 20, 30, and 40 GPa begins after 3620, 3730, and 3900 s,

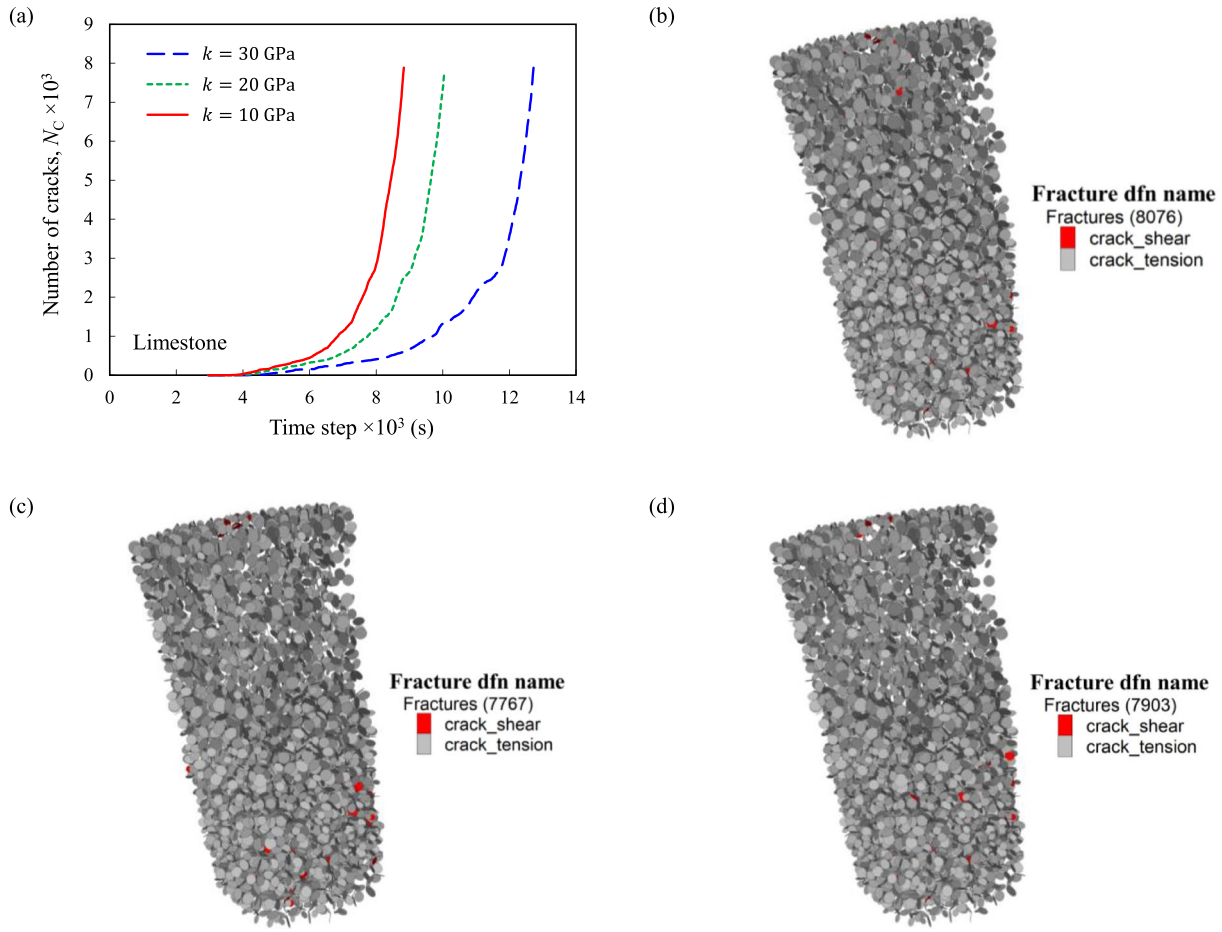

Fig. 12 **a** The effect of stiffness on crack propagation in limestone samples, and fracture distribution in samples with stiffness of **b** 30 GPa, **c** 20 GPa, and **d** 10 GPa

respectively, from the start of the test. At the 7,000 s timestep, the N_c in samples with stiffness levels of 20, 30, and 40 GPa are 2,403, 520, and 314, respectively, indicating a decreasing trend in the N_c with increasing stiffness. Additionally, Fig. 11 indicates that the distribution of cracks in the upper and lower parts of the samples is almost identical, whereas the distribution of cracks in the middle of the model is minimum.

Figure 12 shows the distribution of cracks in the limestone samples, revealing trends consistent with those observed in other materials. As depicted in Fig. 12a, cracking in limestone samples with stiffness values of 10, 20, and 30 GPa begins after 3660, 3820, and 4170 s, respectively, from the start of the test. At the 8,000 s, the N_c in samples with stiffness values of 10, 20, and 30 GPa are 2,630, 1,270, and 410, respectively. Notably, in limestone samples, cracks are present throughout the entire height of the sample but are primarily concentrated in the lower half.

3.2.2 The role of tensile strength

In Fig. 13, the impact of varying tensile strengths on the number and distribution of cracks in granite samples is analyzed. Increasing the F_t results in a significant reduction in the number of cracks. Specifically, at a timestep of 8000 s, samples with tensile strengths of 5, 10, and 15 MPa exhibit 2410, 380, and 200 cracks, respectively. As shown in Fig. 13b, at the highest tensile strength fewer cracks are observed in the lower part of the model, and most of the cracks are concentrated in the upper part. The results also indicate that as F_t increases, the number of tensile cracks significantly decreases, while the number of shear cracks increases. Conversely, with a decrease in F_t, the cracks are predominantly tensile. From a micro-mechanical perspective, tensile stresses tend to pull the particles apart, leading to the formation of tensile cracks. When F_t is high, shear stresses become more significant, leading to an increase in shear cracks as the material begins to

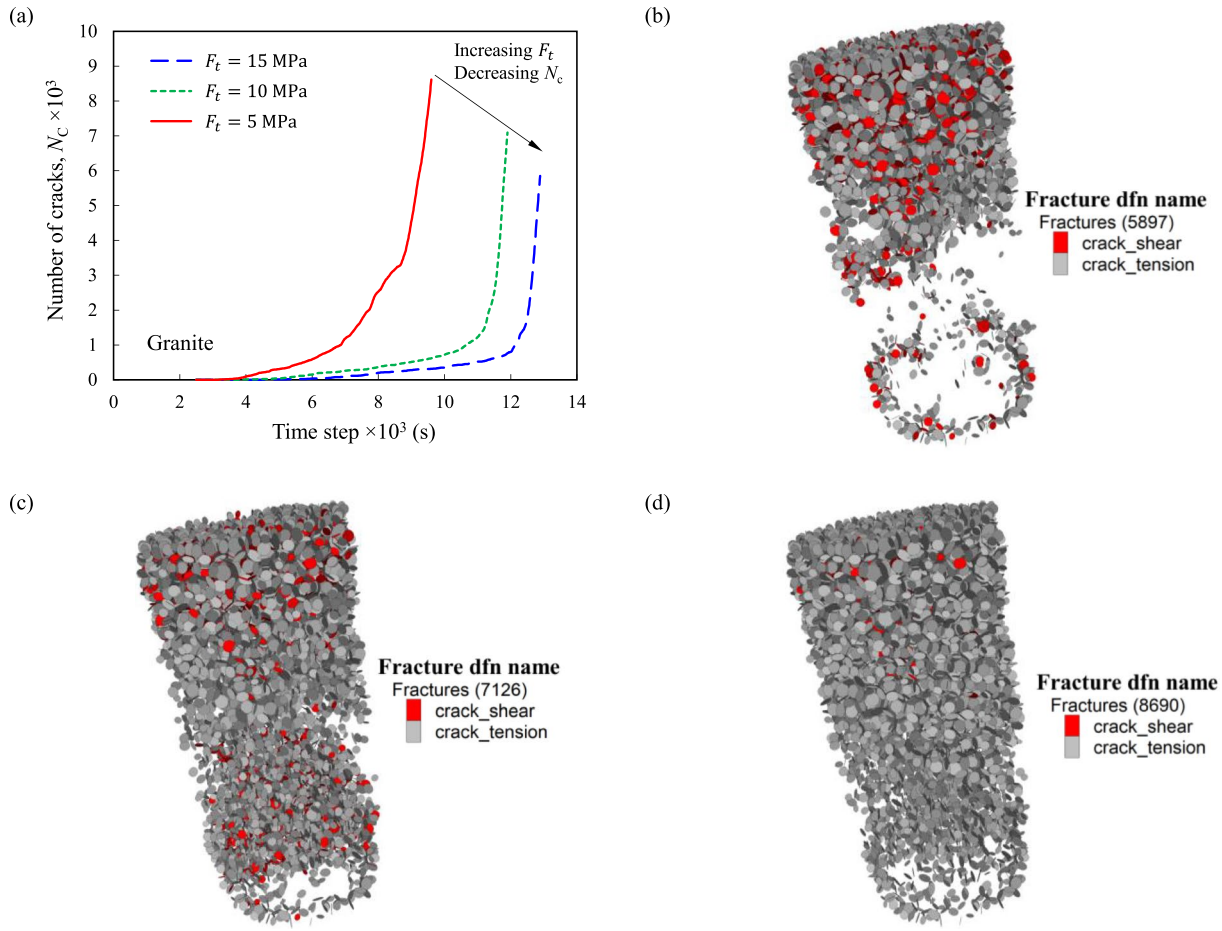

Fig. 13 **a** The effect of tensile strength on crack propagation in granite samples, and fracture distribution in samples with stiffness of **b** 15 MPa, **c** 10 MPa, and **d** 5 MPa

slip along planes of weakness. This behavior highlights the critical role of F_t in governing the transition between tensile-dominated and shear-dominated failure mechanisms in rocks.

Sandstone samples exhibit behavior similar to granite, where an increase in tensile strength leads to a decrease in the N_c. As depicted in Fig. 14, at a timestep of 7000 s, the samples experienced 7290, 490, and 469 cracks at tensile strengths of 2.5, 5, and 7.5 MPa, respectively. Furthermore, at higher tensile strengths, the crack distribution between the upper and lower parts of the sample is nearly identical, whereas the distribution of cracks in the middle of the model is minimum. However, as the tensile strength decreases, the number of shear cracks diminishes, resulting in a crack distribution primarily composed of tensile cracks.

The crack distribution in limestone samples is similar to that observed in other materials, as illustrated in Fig. 15. At the 6000 s timestep, the N_c in samples with tensile strengths of 2, 4, and 6 MPa is 2,510, 335, and 310. A notable difference in limestone is that the number of shear cracks is significantly lower than that of other rocks. In a sample with a tensile strength of 2 MPa, no shear cracks.

Figure 16 compares the $N_{C,max}$ generated in the samples and explores relationships between this parameter and both stiffness and tensile strength. According to Fig. 16a, the proposed relationships for $N_{C,max}$ in granite and sandstone are roughly linear, showing that the maximum number of cracks decreases linearly as stiffness increases. Limestone samples exhibit a unique behavior where the maximum number of cracks decreases initially as stiffness increases, similar to granite and sandstone. This is because at lower stiffness levels, the material behaves more elastically, preventing crack initiation. However, after reaching a certain stiffness threshold, limestone transitions from ductile to brittle failure. At this point, small micro-cracks or defects begin to propagate more rapidly under stress. This shift is due to the material's microstructure, where stress concentrations around defects encourage further crack growth. As a result, the number of

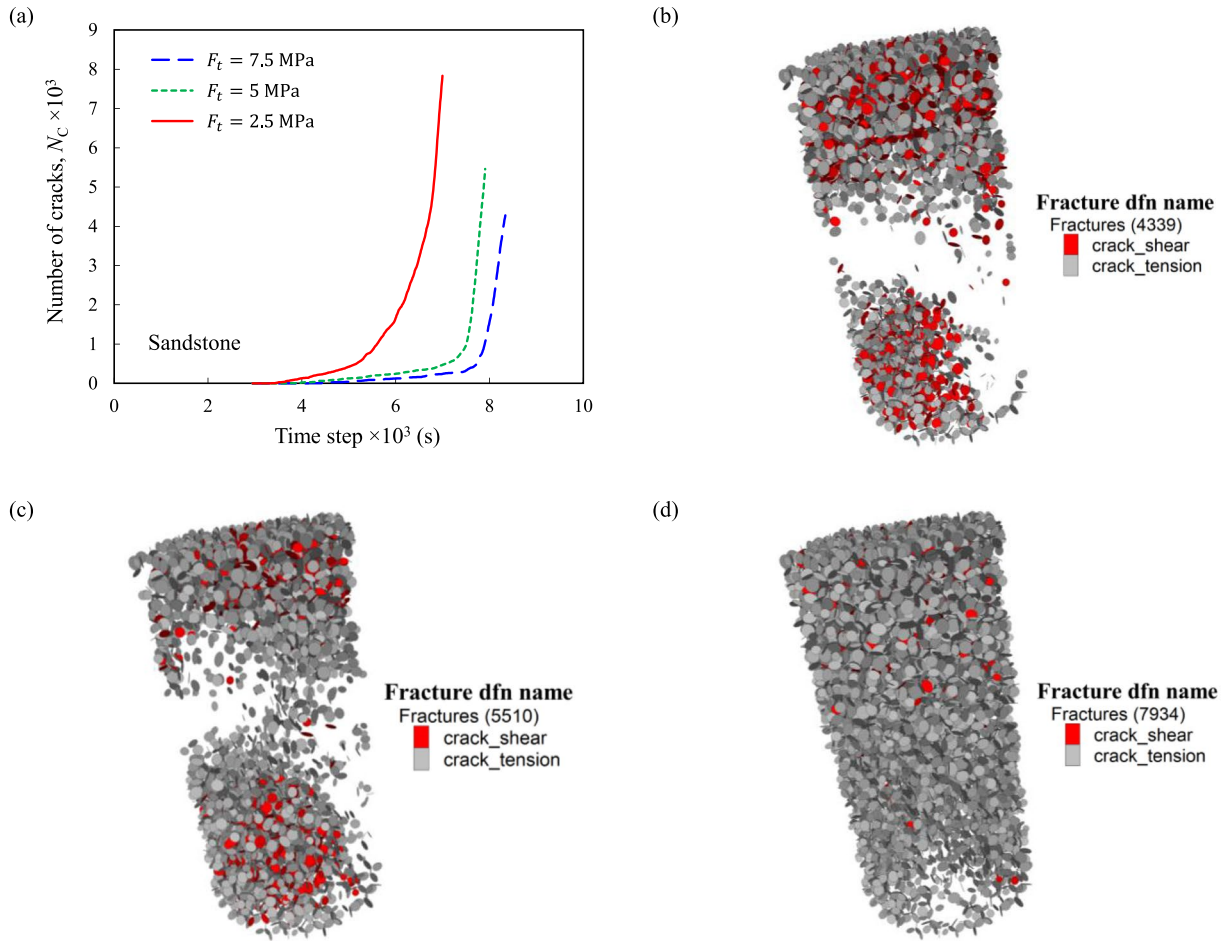

Fig. 14 **a** The effect of tensile strength on crack propagation in sandstone samples, and fracture distribution in samples with stiffness of **b** 7.5 MPa, **c** 5 MPa, and **d** 2.5 MPa

cracks increases beyond the threshold stiffness due to the material's brittle fracture response. According to Fig. 16b, the proposed relationship between $N_{C,max}$ and F_t exhibits a clearer behavior and follows an exponential function.

Overall, a threefold increase in tensile strength resulted in a decrease of 32, 45, and 42% in the maximum number of cracks for granite, sandstone, and limestone, respectively. Sandstone exhibits a more significant reduction in the maximum number of cracks with an increase in tensile strength due to its initial weaker bonding and higher porosity. These features make sandstone more susceptible to cracking under lower loads, so an increase in tensile strength can substantially improve its ability to withstand applied stresses. The results also indicate that the impact of F_t on the cracking which leads to the progressive failure of rock structures is more significant. Specifically, under initial conditions of granite (Table 1), the $N_{C,max}$ in granite is 7098. By increasing the stiffness of granite by 1.4 times, from 50 to 70 GPa, the $N_{C,max}$ decreases to 6760. In contrast, by increasing the tensile strength by 1.5 times, from 10 to 15 MPa, the $N_{C,max}$ decreases from 7098 to 5852.

4 Conclusions

This study conducts grain-scale modeling of rock failure and micro-fracturing under uniaxial compression using the discrete element method, focusing on the influence of stiffness and tensile strength. By examining their role in stress–strain response and the initiation and propagation of tensile and shear cracks, the research provides a micro-mechanical perspective on fracture processes. Simulations were conducted on granite, sandstone, and limestone,

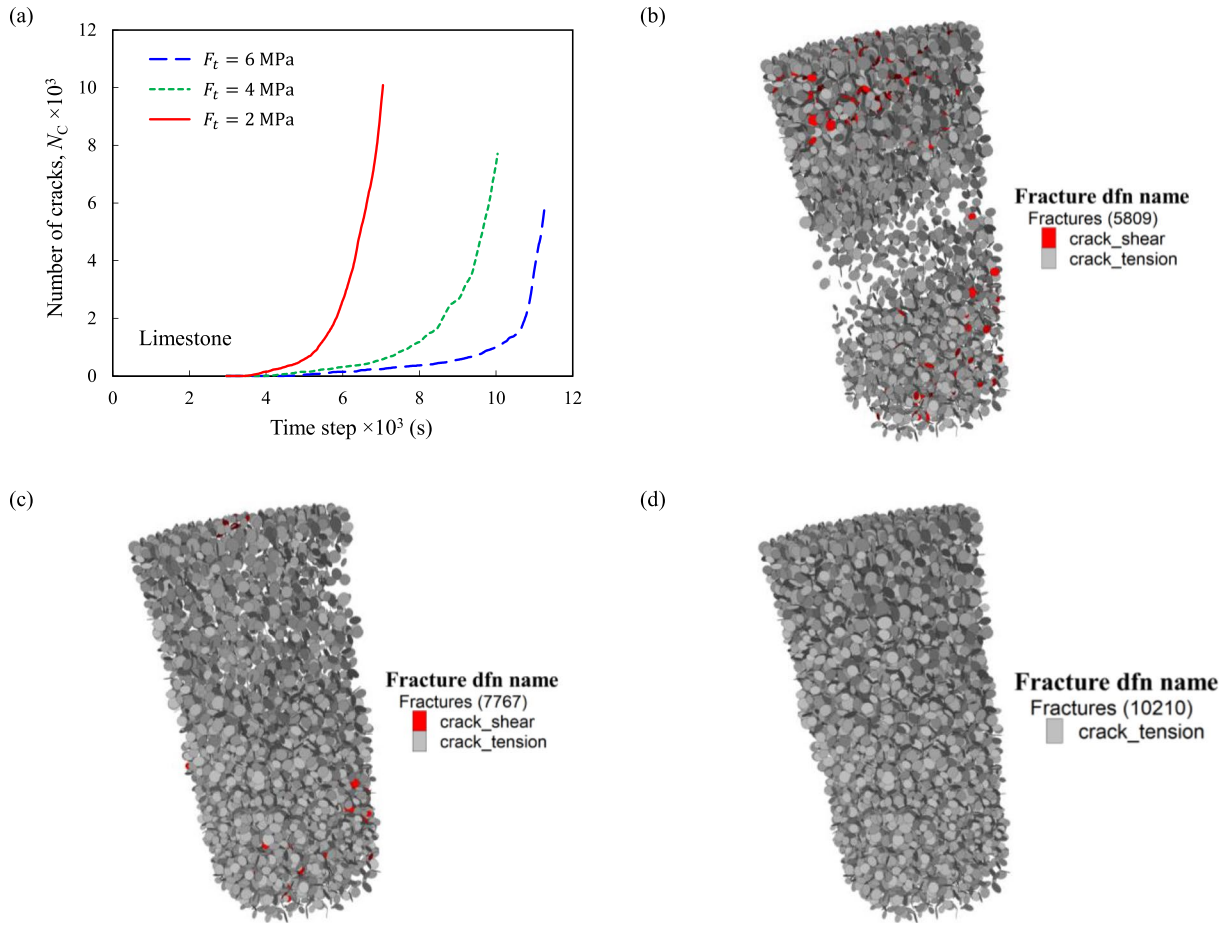

Fig. 15 **a** The effect of tensile strength on crack propagation in limestone samples, and fracture distribution in samples with stiffness of **b** 6 MPa, **c** 4 MPa, and **d** 2 MPa

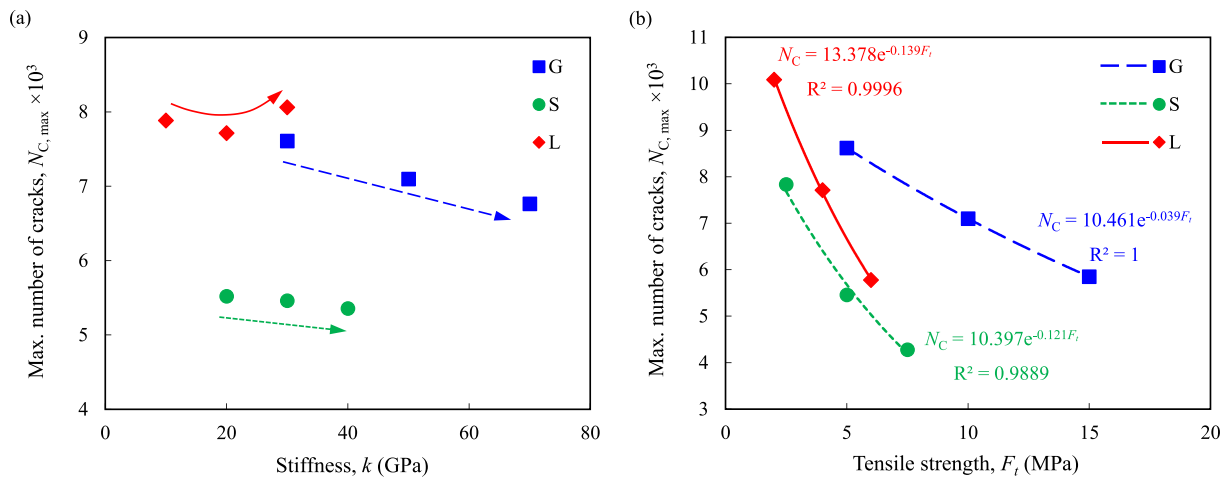

Fig. 16 The dependency of the maximum number of cracks on **a** stiffness and **b** tensile strength

offering detailed insights into their distinct mechanical behaviors. These findings advance our understanding of rock fracture mechanisms and have significant implications for the design and stability analysis of geotechnical structures, where predicting rock behavior under stress is crucial. The findings of this study are as follows:

(1) Granite exhibits the highest peak stress and a steep stress–strain curve due to its interlocking structure and high stiffness. Sandstone, with the lowest peak stress, fails at lower stress levels because of its higher porosity and weaker cohesion. Limestone shows a combination of brittle and ductile failure mechanisms, characterized by significant plastic deformation, a lower peak stress, and a gradual stress–strain curve, resulting in a slower transition from elastic to plastic behavior compared to sandstone.
(2) The stiffness significantly influences the stress–strain behavior of rock samples, with higher stiffness leading to greater final strain values at similar peak stresses. Granite exhibits a 2.25-fold increase in strain with a 2.3-fold stiffness increase, while sandstone and limestone show strain increases of 1.95 and 2.89 times, respectively, with comparable stiffness growth. This relationship shows that higher stiffness increases rocks' ability to withstand greater deformation before failure.
(3) The findings show that higher stiffness reduces deformation under applied loads, allowing rocks to better distribute stress and prevent micro-crack initiation. Stiffer materials have stronger inter-particle bonds, improving overall integrity and resistance to micro-scale failures. As stiffness increases, peak stress remains constant, while peak strain increases, with limestone being more sensitive to stiffness changes than granite.
(4) Increased tensile strength leads to higher stress and strain values at both peak and final points for all rock types. For granite, a threefold increase in tensile strength results in 1.47 times increase in final stress and 1.43 times in final strain. Sandstone shows moderate increases, while limestone exhibits the most significant response, with final stress increasing by 2.46 times and final strain by 2.02 times. This highlights that higher tensile strength delays failure and enhances the rock's ability to withstand greater loads.
(5) Increased stiffness reduces the maximum number of cracks, with granite showing a decrease from 7098 to 6760 when stiffness is increased by 1.4 times. Conversely, increasing tensile strength by 1.5 times results in a larger reduction in crack number, from 7098 to 5852. These results highlight that tensile strength has a greater impact on crack formation than stiffness.

Author contributions All authors contributed to the conceptualization of the study. Z. M. contributed to the numerical modeling, investigation, data collection, validation, visualization, and writing the original draft. M. J. contributed to the investigation, data collection, visualization, and the reviewing and editing of the manuscript.

Data availability The data that support the findings of this study are available from the corresponding author upon reasonable request.

Declarations

Competing interests The authors declare no competing interests.

References

1. Hashemi M, Moghaddas S, Ajalloeian R. Application of rock mass characterization for determining the mechanical properties of rock mass: a comparative study. Rock Mech Rock Eng. 2010;43:305–20. https://doi.org/10.1007/s00603-009-0048-y.
2. Tian Y, Zhou F, Hu L, Liu H. Quantification of rock heterogeneity and application in predicting rock mechanical properties. Bull Eng Geol Env. 2023;82(11):401. https://doi.org/10.1007/s10064-023-03417-8.
3. As'habi F, Lakirouhani A. Numerical modeling of jointed rock samples under unconfined and confined conditions to study peak strength and failure mode. Arab J Geosci. 2021;14(3):174. https://doi.org/10.1007/s12517-021-06569-7.
4. Brady BH, Brown ET. Rock mechanics: for underground mining. Springer science & business media; 2006.

5. He M, Wang Q, Wu Q. Innovation and future of mining rock mechanics. J Rock Mech Geotech Eng. 2021;13(1):1–21. https://doi.org/10.1016/j.jrmge.2020.11.005.
6. Lunardi P, Froldi P, Fornari E. Rock mechanics investigations for rock slope stability assessment. Int J Rock Mech Min Sci Geomech Abstr. 1994;31(4):323–45. https://doi.org/10.1016/0148-9062(94)90901-6.
7. Fan Y, Lu W, Zhou Y, Yan P, Leng Z, Chen M. Influence of tunneling methods on the strainburst characteristics during the excavation of deep rock masses. Eng Geol. 2016;201:85–95. https://doi.org/10.1016/j.enggeo.2015.12.015.
8. Tourchi S, Jabbarzadeh M, Sadeghi H, Lavasan AA. Thermo-hydro-mechanical modelling of rock cliff-atmosphere interaction: the case of the Pozary test site in Czechia. In: No. EGU24-20407), Copernicus Meetings. 2024. https://doi.org/10.5194/egusphere-egu24-20407.
9. Fjaer E, Holt RM, Horsrud P, Raaen AM. Petroleum related rock mechanics. Elsevier; 2008.
10. Sachsenhofer RF, Popov SV, Coric S, Mayer J, Misch D, Morton MT, Pupp M, Rauball J, Tari G. Paratethyan petroleum source rocks: an overview. J Pet Geol. 2018;41(3):219–45. https://doi.org/10.1111/jpg.12702.
11. Tourchi S, Jabbarzadeh M, Lavasan AA, Sadeghi H, Racek O. Thermo-hydro-mechanical dynamics of a rock slope: integrated field and numerical analysis at the Požáry test site in the Czech Republic. J Rock Mech Geotech Eng. 2024. https://doi.org/10.1016/j.jrmge.2024.09.052.
12. Tourchi S, Jabbarzadeh M, Sadeghi H. Thermo-hydro-mechanical analysis of soil strata suffered from desiccation cracking. In: Geotechnical engineering challenges to meet current and emerging needs of society. London: CRC Press; 2024. p. 1362–7. https://doi.org/10.1201/9781003431749-249.
13. Sadeghi H, Jabbarzadeh M, Tourchi S. Thermo-hydro-mechanical modelling of the heterogeneous subsidence and swelling in the desiccation cracked clayey strata. Eng Geol. 2024;343:107798. https://doi.org/10.1016/j.enggeo.2024.107798.
14. Jabbarzadeh M, Sadeghi H, Tourchi S, Darzi AG. Thermo-hydraulic analysis of desiccation cracked soil strata considering ground temperature and moisture dynamics under the influence of soil-atmosphere interactions. Geomech Energy Environ. 2024;38:100558. https://doi.org/10.1016/j.gete.2024.100558.
15. Ghandilou MJ, Tourchi S, Sadeghi H. Numerical investigation of cyclic wetting and drying of Boom clay based on the Barcelona Expansive Model. In: 84th EAGE annual conference & exhibition (Vol. 2023, No. 1). European Association of Geoscientists & Engineers; 2023. p. 1–5. https://doi.org/10.3997/2214-4609.202310400.
16. Valipour M, Jabbarzadeh M, Sadeghi H, Roghangar K. Volumetric behavior of a soil column subjected to freeze-thaw cycles under coupled thermo-hydro-mechanical conditions. GeoMontréal. 2024. https://www.researchgate.net/publication/384431981.
17. Mousavi Z, Jafarzadeh F. The influence of gradation on shear behavior of Glass Beads: a DEM study. In: 14th national congress on civil engineering. 2024. https://www.researchgate.net/publication/380667931.
18. Bieniawski ZT. Estimating the strength of rock materials. J South Afr Inst Min Metall. 1974;74(8):312–20.
19. Griffith AAVI. The phenomena of rupture and flow in solids. Phil Trans R Soc Lond. 1921;221(582–593):163–98. https://doi.org/10.1098/rsta.1921.0006.
20. Main IG, Sammonds PR, Meredith PG. Application of a modified Griffith criterion to the evolution of fractal damage during compressional rock failure. Geophys J Int. 1993;115(2):367–80. https://doi.org/10.1111/j.1365-246X.1993.tb01192.x.
21. Asemi F, Lakirouhani A, Nicksiar M, Zohdi A. A new rock brittleness index based on crack initiation and crack damage stress thresholds. Int J Geomech. 2024;24(5):04024074. https://doi.org/10.1061/IJGNAI.GMENG-9151.
22. Li L, Hu J, Li S, Qin C, Liu H, Chen D, Wang J. Development of a novel triaxial rock testing method based on biaxial test apparatus and its application. Rock Mech Rock Eng. 2021;54:1597–607. https://doi.org/10.1007/s00603-020-02329-3.
23. Shen J, Jimenez R, Karakus M, Xu C. A simplified failure criterion for intact rocks based on rock type and uniaxial compressive strength. Rock Mech Rock Eng. 2014;47:357–69. https://doi.org/10.1007/s00603-013-0408-5.
24. Zhang HY, Xu WJ, Yu YZ. Triaxial tests of soil–rock mixtures with different rock block distributions. Soils Found. 2016;56(1):44–56. https://doi.org/10.1016/j.sandf.2016.01.004.
25. Huang D, Gu D, Yang C, Huang R, Fu G. Investigation on mechanical behaviors of sandstone with two preexisting flaws under triaxial compression. Rock Mech Rock Eng. 2016;49:375–99. https://doi.org/10.1007/s00603-015-0757-3.
26. Aladejare AE. Evaluation of empirical estimation of uniaxial compressive strength of rock using measurements from index and physical tests. J Rock Mech Geotech Eng. 2020;12(2):256–68. https://doi.org/10.1016/j.jrmge.2019.08.001.
27. Aladejare AE, Alofe ED, Onifade M, Lawal AI, Ozoji TM, Zhang ZX. Empirical estimation of uniaxial compressive strength of rock: database of simple, multiple, and artificial intelligence-based regressions. Geotech Geol Eng. 2021;39:4427–55. https://doi.org/10.1007/s10706-021-01772-5.
28. Scholtès L, Donzé FV. A DEM model for soft and hard rocks: role of grain interlocking on strength. J Mech Phys Solids. 2013;61(2):352–69. https://doi.org/10.1016/j.jmps.2012.10.005.
29. Zhang C, Tu S, Bai Q. Evaluation of pore size and distribution impacts on uniaxial compressive strength of lithophysal rock. Arab J Sci Eng. 2018;43:1235–46. https://doi.org/10.1007/s13369-017-2810-x.
30. Xie L, Jin P, Su TC, Li X, Liang Z. Numerical simulation of uniaxial compression tests on layered rock specimens using the discrete element method. Comp Part Mech. 2020;7:753–62. https://doi.org/10.1007/s40571-019-00307-3.
31. Zheng Z, Tang H, Zhang Q, Pan P, Zhang X, Mei G, Liu Z, Wang W. True triaxial test and PFC3D-GBM simulation study on mechanical properties and fracture evolution mechanisms of rock under high stresses. Comput Geotech. 2023;154:105136. https://doi.org/10.1016/j.compgeo.2022.105136.
32. Zheng Z, Li S, Zhang Q, Tang H, Liu G, Pei S, Lu G. True triaxial test and DEM simulation of rock mechanical behaviors, meso-cracking mechanism and precursor subject to underground excavation disturbance. Eng Geol. 2024;337:107567. https://doi.org/10.1016/j.enggeo.2024.107567.
33. Hudson JA, Harrison JP. Engineering rock mechanics: an introduction to the principles. Elsevier; 2000.
34. Lakirouhani A, Asemi F, Zohdi A, Medzvieckas J, Kliukas R. Physical parameters, tensile and compressive strength of dolomite rock samples: influence of grain size. J Civ Eng Manag. 2020;26(8):789–99. https://doi.org/10.3846/jcem.2020.13810.
35. Fairhurst C. On the validity of the 'Brazilian' test for brittle materials. Int J Rock Mech Min Sci Geomech Abstr. 1964;1(4):535–46. https://doi.org/10.1016/0148-9062(64)90060-9.

36. Lockner D. The role of acoustic emission in the study of rock fracture. Int J Rock Mech Min Sci Geomech Abstr. 1993;30(7):883–99. https://doi.org/10.1016/0148-9062(93)90041-B.
37. Miao S, Pan PZ, Yu P, Zhao S, Shao C. Fracture analysis of Beishan granite after high-temperature treatment using digital image correlation. Eng Fract Mech. 2020;225:106847. https://doi.org/10.1016/j.engfracmech.2019.106847.
38. Wyllie DC, Mah C. Rock slope engineering. CRC Press; 2004.
39. Potyondy DO, Cundall PA. A bonded-particle model for rock. Int J Rock Mech Min Sci. 2004;41(8):1329–64. https://doi.org/10.1016/j.ijrmms.2004.09.011.
40. Potyondy DO. Parallel-bond refinements to match macroproperties of hard rock. In: Sainsbury D, Hart R, Detournay C, Nelson M, editors. Continuum and distinct element numerical modeling in geomechanics, proceedings of second international FLACDEM symposium, Melbourne, Australia; 2011. p. 459–65. ISBN 978-0-9767577-2-6. Minneapolis Itasca International.
41. ASTM. Standard test methods for compressive strength and elastic moduli of intact rock core specimens under varying states of stress and temperatures. ASTM D7012-23. 10.1520/D7012-23. 2023.
42. Tuncay E, Hasancebi N. The effect of length to diameter ratio of test specimens on the uniaxial compressive strength of rock. Bull Eng Geol Env. 2009;68:491–7. https://doi.org/10.1007/s10064-009-0227-9.
43. Li XB, Lok TS, Zhao J. Dynamic characteristics of granite subjected to intermediate loading rate. Rock Mech Rock Eng. 2005;38:21–39. https://doi.org/10.1007/s00603-004-0030-7.
44. Sano O, Kudo Y, Mizuta Y. Experimental determination of elastic constants of oshima granite, barre granite, and chelmsford granite. J Geophys Res Solid Earth. 1992;97(B3):3367–79. https://doi.org/10.1029/91JB02934.
45. Labuz JF, Shah SP, Dowding CH. Experimental analysis of crack propagation in granite. Int J Rock Mech Min Sci Geomech Abstr. 1985;22(2):85–98. https://doi.org/10.1016/0148-9062(85)92330-7.
46. Zhou Z, Cai X, Ma D, Chen L, Wang S, Tan L. Dynamic tensile properties of sandstone subjected to wetting and drying cycles. Constr Build Mater. 2018;182:215–32. https://doi.org/10.1016/j.conbuildmat.2018.06.056.
47. Zhao Z, Yang J, Zhang D, Peng H. Effects of wetting and cyclic wetting–drying on tensile strength of sandstone with a low clay mineral content. Rock Mech Rock Eng. 2017;50:485–91. https://doi.org/10.1007/s00603-016-1087-9.
48. Zhou Z, Cai X, Chen L, Cao W, Zhao Y, Xiong C. Influence of cyclic wetting and drying on physical and dynamic compressive properties of sandstone. Eng Geol. 2017;220:1–12. https://doi.org/10.1016/j.enggeo.2017.01.017.
49. Schmidt RA. Fracture-toughness testing of limestone: KIc of indiana limestone was measured using three-point-bend specimens, and toughness is seen to increase with crack length much like many aluminum alloys. Exp Mech. 1976;16(5):161–7. https://doi.org/10.1007/BF02327993.
50. Golewski GL. Effect of coarse aggregate grading on mechanical parameters and fracture toughness of limestone concrete. Infrastructures. 2023;8(8):117. https://doi.org/10.3390/infrastructures8080117.
51. Al-Shayea NA, Khan K, Abduljauwad SN. Effects of confining pressure and temperature on mixed-mode (I–II) fracture toughness of a limestone rock. Int J Rock Mech Min Sci. 2000;37(4):629–43. https://doi.org/10.1016/S1365-1609(00)00003-4.
52. Wawersik WR, Fairhurst CH. A study of brittle rock fracture in laboratory compression experiments. Int J Rock Mech Min Sci Geomech Abstr. 1970;7(5):561–75. https://doi.org/10.1016/0148-9062(70)90007-0.
53. Stavrogin AN, Tarasov BG, Shirkes OA, Pevzner ED. Strength and deformation of rocks before and after the breakdown point. Soviet Min. 1981;17(6):487–93. https://doi.org/10.1007/BF02497983.
54. Li C, Prikryl R, Nordlund E. The stress-strain behaviour of rock material related to fracture under compression. Eng Geol. 1998;49(3–4):293–302. https://doi.org/10.1016/S0013-7952(97)00061-6.
55. Li S, Lajtai EZ. Modeling the stress–strain diagram for brittle rock loaded in compression. Mech Mater. 1998;30(3):243–51. https://doi.org/10.1016/S0167-6636(98)00052-0.
56. Shan R, Jiang Y, Li B. Obtaining dynamic complete stress–strain curves for rock using the split Hopkinson pressure bar technique. Int J Rock Mech Min Sci. 2000;37(6):983–92. https://doi.org/10.1016/S1365-1609(00)00031-9.
57. Zhou XP, Zhang YX, Ha QL, Zhu KS. Micromechanical modelling of the complete stress–strain relationship for crack weakened rock subjected to compressive loading. Rock Mech Rock Eng. 2008;41:747–69. https://doi.org/10.1007/s00603-007-0130-2.
58. Esmaeili K, Hadjigeorgiou J, Grenon M. Capturing the complete stress–strain behaviour of jointed rock using a numerical approach: stress–strain behavior of jointed rock. Int J Numer Anal Methods Geomech. 2015;39(10):1027–44. https://doi.org/10.1002/nag.2346.
59. Meng F, Zhou H, Zhang C, Xu R, Lu J. Evaluation methodology of brittleness of rock based on post-peak stress–strain curves. Rock Mech Rock Eng. 2015;48:1787–805. https://doi.org/10.1007/s00603-014-0694-6.
60. Zhang CL. The stress–strain–permeability behaviour of clay rock during damage and recompaction. J Rock Mech Geotech Eng. 2016;8(1):16–26. https://doi.org/10.1016/j.jrmge.2015.10.001.
61. Wang Y, Li CH, Hu YZ, Zhou XL. A new method to evaluate the brittleness for brittle rock using crack initiation stress level from uniaxial stress–strain curves. Environ Earth Sci. 2017;76:1–18. https://doi.org/10.1007/s12665-017-7117-4.
62. Liu D, He M, Cai M. A damage model for modeling the complete stress–strain relations of brittle rocks under uniaxial compression. Int J Damage Mech. 2018;27(7):1000–19. https://doi.org/10.1177/1056789517720804.
63. Zhou H, Chen J, Lu J, Jiang Y, Meng F. A new rock brittleness evaluation index based on the internal friction angle and class I stress–strain curve. Rock Mech Rock Eng. 2018;51:2309–16. https://doi.org/10.1007/s00603-018-1487-0.
64. Liu C, Du L, Zhang X, Wang Y, Hu X, Han Y. A new rock brittleness evaluation method based on the complete stress-strain curve. Lithosphere. 2021;2021(Special 4):4029886. https://doi.org/10.2113/2021/4029886.
65. Kuang Z, Qiu S, Li S, Du S, Huang Y, Chen X. A new rock brittleness index based on the characteristics of complete stress–strain behaviors. Rock Mech Rock Eng. 2021;54:1109–28. https://doi.org/10.1007/s00603-020-02311-z.